Mapping of Dynamics between Mechanical and Electrical Ports in SG-IBR Composite Grids

Yitong Li, *Member, IEEE*, Yunjie Gu, *Senior Member, IEEE*, Timothy C. Green, *Fellow, IEEE*

***Abstract*—Power grids are traditionally dominated by synchronous generators (SGs) but are currently undergoing a major transformation due to the increasing integration of inverter-based resources (IBRs). The state space method with transparent apparatus models can be readily used. However, models of IBRs are usually not disclosed by manufacturers. Alternatively, the port-based approach represents dynamics by input-output transfer functions without exposing internal states. These transfer functions at various ports are normally configured with a particular focus: an SG-dominated grid is traditionally analyzed in a *mechanical-centric* view which ignores fast electrical dynamics and focuses on the torque-speed dynamics, whereas the emergent IBR-dominated grid usually takes an *electrical-centric* view which focuses on the voltage-current interaction. In this article, a new perspective called the *port-mapping method* is proposed to combine these two views. Specifically, the mechanical dynamics are mapped to the electrical impedance seen at the electrical port; and the electrical dynamics are also mapped to the torque coefficient seen at the mechanical port. The bidirectional mapping gives additional flexibility and insights to analyze the sub-system interactions in whole-system dynamics and guide the tuning of parameters. Application of the proposed method is illustrated in three cases with increasing scales.**

***Index Terms*—Port-Mapping, Electrical-Mechanical Two-Port Network, Synchronous Generator, Inverter Based Resource, Composite Power System**

I. INTRODUCTION

Power systems have traditionally been dominated by synchronous generators (SGs) [1], [2]. In recent years, due to the drive towards renewable energy, power electronics and inverter-based resources (IBRs) have become increasingly common features of the power system [3]–[5], and thus the power system is being transformed from SG-dominated to SG-IBR composite. This structural change results in new oscillation modes and the emergence of new stability problems [5]–[10]. Analyzing the system dynamics is the first step to addressing the new challenges emerging to system stability. The classic state-space approach can be readily extended to a SG-IBR composite grid [7], [11], but this effort is often compromised in practice by the lack of transparent models (also known as white-box models) since the internal control dynamics of IBRs are usually not disclosed nor standardised by manufacturers. To address this issue, the port-based approach (also known as black-box analysis) has recently gained attention. This approach represents the dynamics of a system via the input-output transfer function at a port without exposing the internal states, and therefore circumvents the need for transparent models.

There are multiple choices available on the position where a port is opened in a system and this creates multiple perspectives useful in understanding stability issues. Before the emergence of IBRs, a *mechanical-centric* view was adopted following the tradition of mechanical engineers: ports are opened on the shafts of SGs and a dynamic relationship is represented by torque-speed (T-ω) interaction. The electrical network is transformed to a mechanical representation of torque coefficients to fit into the mechanical ports, as illus-

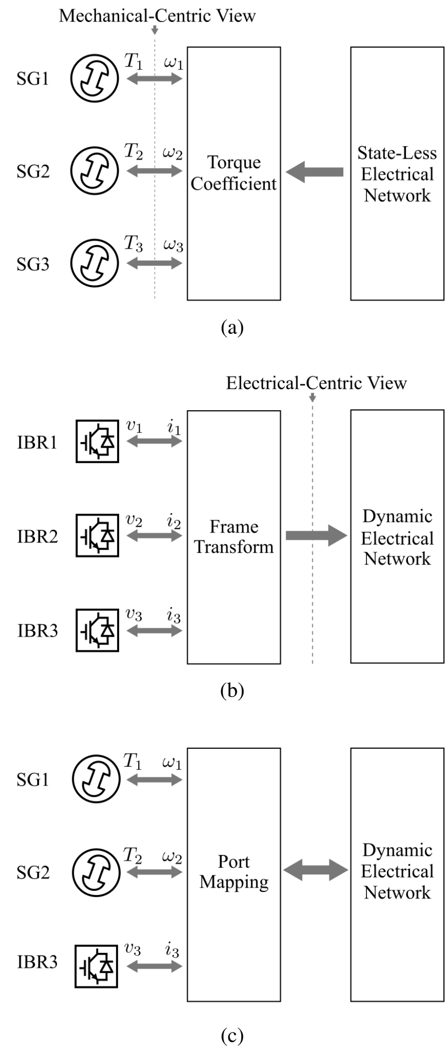

Fig. 1. Power system analysis framework. (a) Mechanical-centric view of SG-dominated systems, where T and ω are torque and rotor speed respectively. (b) Electrical-centric view of IBR-dominated power systems, where v and i are voltage and current respectively. (c) Port-mapping view of SG-IBR composite power systems. Throughout the article, we use "network" to represent electrical transmission lines, and use "grid" to represent network plus apparatus (generators, inverters, and so on).

trated in Fig. 1 (a) [1], [9]. This perspective has been very successful in investigating the torsional and swing dynamics SGs, but the fast electrical dynamics (e.g. the decay of flux and resonance of inductance and capacitance) are truncated in torque coefficients, meaning that it is not applicable when fast electromagnetic transients (EMTs) are of concern. On the other hand, the rise of IBRs brings about an *electrical-centric* view following the tradition of electronic engineers: ports are opened on electrical circuits and a dynamic relationship is represented by voltage-current (v-i) interaction, as shown in Fig. 1 (b) [12]–[18]. This view is widely known as the impedance-based approach and has been very successful in investigating the harmonic stability of IBRs. However, it is not straightforward to represent the mechanical dynamics of SGs (angle, speed, and inertia acceleration) at electrical ports so the impedance-based approach has been limited to IBRs connected to infinite buses where the frequency (rotation speed) is held constant.

It is clear that neither port-approach fully captures the important features of SG-IBR composite grids where EMT and mechanical rotational dynamics both play significant roles and may interact in whole-system dynamics. Therefore, a framework to link the mechanical and electrical ports is desired. The fundamental difficulty in establishing a unified port-based view is that frame transformations are needed to align the mechanical angles of the various SGs and the phase-locked angles of the various IBRs in the dynamic electrical network. The frame transformations themselves contain dynamics meaning that SG and IBR in different frames cannot be directly connected [11]. To address this difficulty, a method called frame dynamics embedding is proposed in [17] where the rotational dynamics in the frame transformation are embedded into the electrical ports, making them frame-independent. The frame dynamics embedding method is applied to both SGs and IBRs, yielding impedance element models where the mechanical rotors and the phase-locked loops can be represented as equivalent electrical elements [16], [17], [19].

In this article, we extend the approach in [17] with a bidirectional mapping of dynamics between mechanical and electrical ports, yielding a full-fledged framework for port-based modelling of SG-IBR composite grids, as illustrated in Fig. 1(c). Both EMT and rotational dynamics are preserved at all ports, but different oscillation modes may have different observability at each port. Probing at multiple ports yields knowledge of the root-cause of oscillations and potential stabilisation schemes. The port-mapping method can also be generalised to other ports, such as the dc-links and phase-locked loops (PLLs) in IBRs and the exciters in SGs.

The bidirectional port-mapping proposed in this article offers benefits in stability analysis. For example, the conventional torque coefficient, which ignores electrical dynamics, would fail to predict system instability when the line resistance is large or when the oscillation frequency is high. This problem is solved by mapping the electrical dynamics to a mechanical port, which yields the new concept of *dynamic torque coefficient*. Via this concept, we reflects electrical dynamics on a mechanical port, and show that the positive damping on electrical ports may be mapped to negative damping on mechanical ports, which is invisible in impedance-based models alone [17]. This phenomenon is named *double-edged damping* to raise attention to the potential contradiction of damping at different ports. Further to the dynamic torque coefficient, we develop the concept of *dc-current coefficient* (i.e., generalized torque coefficient) by mapping the rotational and EMT dynamics into the dc-link port of an IBR, which offers new explanations for IBR interaction with weak grids. Additionally, the proposed port method is also applied to a multi-apparatus grid, to identify the participation of each apparatus in critical oscillation modes, and does so without the need for the transparent models of the state space method.

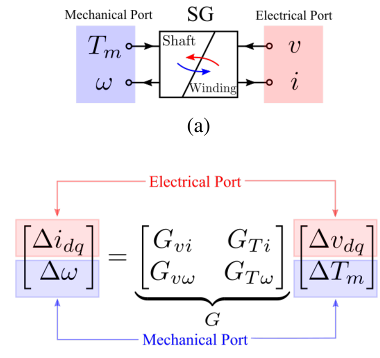

Fig. 2. Two-port model of SG. (a) Port-mapping flow. (b) Transfer function model.

The article is organized as follows. In Section II, the concept of port-mapping is introduced and the detailed modelling procedure is illustrated on a SG and a IBR. Section III links the port-based models in a SG-IBR composite grid to show the extra flexibility and insights provided by the proposed method in system dynamic analysis. Section IV demonstrated the proposed method in three case studies. Section V concludes the article.

II. The Port-Mapping Method

In this section, we introduce the fundamentals of the port-mapping method via the examples of a SG and an IBR.

A. Mechanical-Electrical Two-Port Network

Inspired by the two-port network theory in electrical circuits [20], we represent a SG as a mechanical-electrical two-port model as shown in Fig. 2. The mechanical port captures the mechanical dynamics by a transfer function between mechanical torque T_m and rotor speed ω through the rotor shaft, i.e., a *mechanical impedance*; The electrical port captures the electrical dynamics by a transfer function between terminal voltage v and current i through stator windings, i.e., a electrical impedance. The two ports interact with each other via electrical-mechanical coupling between the rotor and the stator. The mathematical description of the mechanical-electrical two-port network can be formulated as a transfer function matrix G whose diagonal elements represent the self dynamics of a port and the off-diagonal elements represent cross-port coupling, as illustrated in Fig. 2 (b). The transfer function (or equivalently a frequency spectrum) can be readily obtained by mathematical derivation if the detailed state space model is known, such as that in Appendix A. In practice, the transfer function would probably be provided or measured by manufacturers who do not want to disclose the detailed control algorithms and state equations and is thus a form of black-box modeling.

The mechanical-electrical two-port model provides a general step for cross-domain modelling but there are difficulties to overcome before these modular models can be used in whole-system analysis. As shown in Fig. 3 (a), the model of a SG is presented in its local dq reference frame aligned to its rotor, which needs to be aligned to a global electrical reference frame DQ when the electrical ports of multiple apparatuses are linked in a grid. The DQ frame is called the global steady frame which rotates with a constant angular frequency so that it is "dynamically neutral", that is, does not contain frame dynamics in itself [17]. The frame alignment from dq to DQ contains dynamics in itself which is usually represented as extra global synchronising signals [11] but this causes the linked whole-system model lose its modularity. To solve this problem, we transform the electrical port to the global DQ frame and map the frame dynamics into the port matrix so that no extra global synchronisation signals are needed and the whole-system model retains modularity, as described in the following sub-section.

B. Mapping of Mechanical Dynamics to Electrical Ports

Our approach is based on a key observation that the mechanical dynamics of the rotor is identical to the frame dynamics of the electrical port, which offer a bridge for dynamic mapping across mechanical-electrical ports, as illustrated conceptually in the port-mapping flow in Fig. 3 (c) and shown in detail in the block diagram in Fig. 3 (e). We now give the mathematical details. The transformation from mechanical frame dq to global frame DQ for an arbitrary signal u can be represented using the transformation matrix T_ϵ as

$$\underbrace{\begin{bmatrix} u_D \\ u_Q \end{bmatrix}}_{u_{DQ}} = \underbrace{\begin{bmatrix} \cos\epsilon & -\sin\epsilon \\ \sin\epsilon & \cos\epsilon \end{bmatrix}}_{T_\epsilon} \underbrace{\begin{bmatrix} u_d \\ u_q \end{bmatrix}}_{u_{dq}} \tag{1}$$

where ϵ is the angle difference between dq and DQ as indicated in Fig. 3 (a). By linearizing this equation, we get

$$\underbrace{\begin{bmatrix} \Delta u_D \\ \Delta u_Q \end{bmatrix}}_{\Delta u_{DQ}} = T_{\epsilon_0}\left(\underbrace{\begin{bmatrix} \Delta u_d \\ \Delta u_q \end{bmatrix}}_{\Delta u_{dq}} + \underbrace{\begin{bmatrix} -u_{q0} \\ u_{d0} \end{bmatrix}}_{U_0} \Delta\epsilon \right) \tag{2}$$

where the subscript 0 denotes steady-state operating points and the prefix Δ denotes perturbation around the operating points. The angle perturbation $\Delta\epsilon$ is the integration of the mechanical speed, that is, $\Delta\epsilon = \Delta\omega/s$ where s is Laplace operator so $1/s$ represents integration. This relationship is indicated by the blue arrows in the block diagram Fig. 3 (e) and yields the transformation from G to G', where the electrical port of G' is represented in the global DQ frame so that it can be readily linked with other apparatuses in the electrical network. The detailed process of the transformation and the element-wise value of G' can be found in Appendix B-A. The transformed electrical impedance G_{vi} in G' has identical properties and consequences to the frame-dynamics embedding method in [17]. But notably, this dynamics embedding also influences the mechanical impedance $G_{T\omega}$ in G' because of the internal coupling between mechanical and electrical ports of the SG itself, as visualized by the small blue and red arrows inside the SG block in Fig. 3(c) and as derived in Appendix B-A. This also implies the difference between the bidirectional mapping of dynamics in this article and the unidirectional mapping in [17].

C. Mapping of Electrical Dynamics to Mechanical Ports

In the mechanical-electrical two-port model G' the terminal voltage v_{DQ} is taken as an independence input. In reality, v_{DQ} is also affected by the current i_{DQ} via the equivalent impedance Z_b seen at the bus where the apparatus is connected. This yields an extra loop in the block diagram as indicated by the red arrow in Fig. 3 (e). Closing this loop yields the transformation from G' to G'' where the electrical impedance of the grid Z_b is mapped into the two-port network. It should be noted that input voltage of G'' is changed from v_{DQ} to v_{bDQ} which is the equivalent voltage of the grid behind Z_b. The detailed process of the transformation and the element-wise value of G'' can be found in Appendix B-B. Again, all four elements of G' are changed during this procedure.

It is worth noting that the mapping procedures in this and last subsections only require the prior knowledge of transfer functions at different ports of an apparatus rather than its detailed state equations, which preserves the black-box feature.

D. Generalising to IBR

The port-mapping methodology for a SG discussed in the previous sub-sections can be readily generalised to other apparatuses, such as an IBR, as illustrated in the right column in Fig. 3. An IBR (grid-following) has a rotating angle in its phase-locked loop (PLL) which is used for synchronisation. The active power is regulated by the balancing of the dc-link voltage. The PLL and the dc-link in a grid following IBR roughly have the same function as the rotor in a SG, for synchronisation and power balancing. Therefore, an IBR is a three-port apparatus where the PLL and dc-link port jointly serve as a virtual mechanical port. The port-mapping transformation from G to G' and to G'' for an IBR can be obtained easily from the block diagrams in Fig. 3 (f).

III. Port-Based Analysis of SG-IBR Composite Grids

Having established a step-by-step procedure for dynamic mapping across ports in a SG and a IBR, we now use the derived port-based model to examine the stability of SG-IBR composite grids.

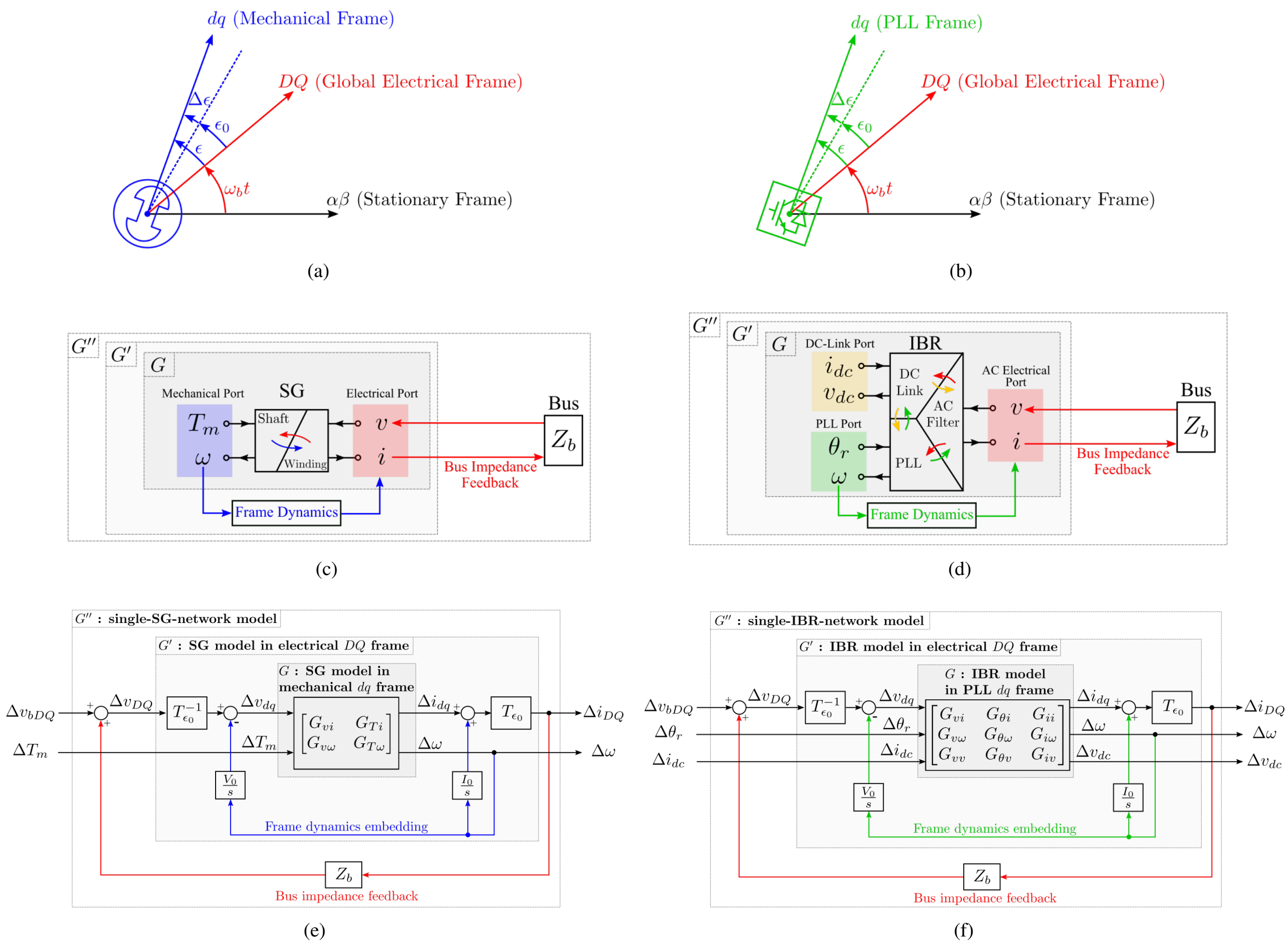

Fig. 3. Analyzing single-apparatus-infinite-bus system by port-mapping method. (a) Frame illustration of SG. (b) Frame illustration of IBR. (c) Port-mapping flow of SG. (d) Port-mapping flow of IBR. (e) Block diagram of SG. (f) Block diagram of IBR.

A. Linking SG-IBR Composite Grids

We first link the port-based SG and IBR models in a composite grid. Taking the grid in Fig. 4 as an example, the corresponding block diagram is shown in Fig. 5. The port matrix G for each apparatus is transformed to G' (this is done locally without knowledge on the whole grid), and then appended on G'_N to represent the joint port matrices of all apparatuses. G'_N interact with the network impedance matrix Z_{bN} to form the whole-system port model G''_N. Z_{bN} is the inversion of nodal admittance matrix Y_{bN} [17] rather than a simple branch impedance. Z_{bN} is dynamic impedance formulated in the s-domain (not simply $R + jX$) so all EMT dynamics are preserved. The entire procedure for port-mapping and port-based modelling are summarized in the model derivation tree in Fig. 6 to facilitate the readers.

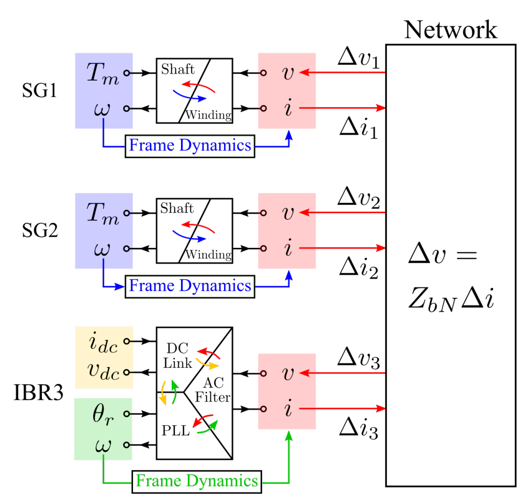

Fig. 4. Port-mapping flow for a SG-IBR Composite power grid.

B. Port-Based System Bipartition

Now we explain the benefits of the port-mapping approach in whole-system stability studies. System bipartition is commonly used to investigate the interaction of sub-systems in a power system. For example, in the electrical-centric view, a power system is separated into sources and loads and their interaction is characterised by the impedance ratio between the source part and load part. This bipartition method can

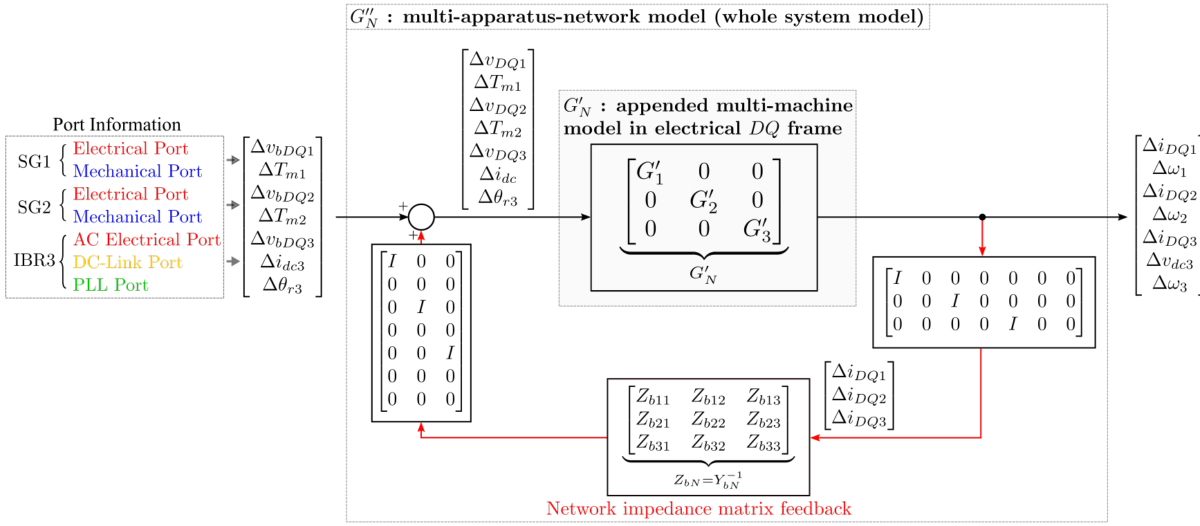

Fig. 5. Block diagram for the SG-IBR composite power grid in Fig. 4.

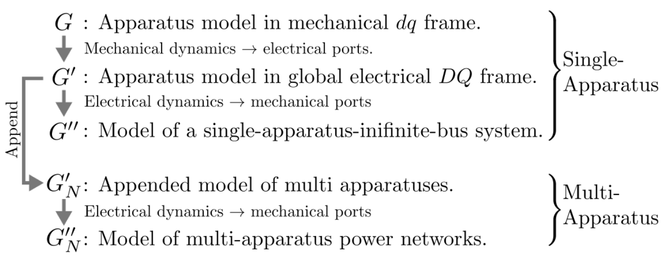

Fig. 6. Model derivation tree: the procedure to get single-apparatus and multi-apparatus port matrices.

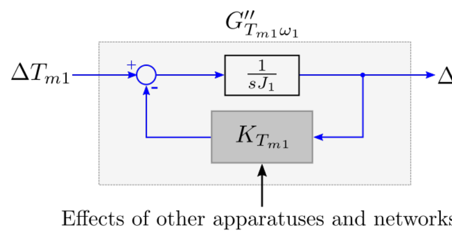

Fig. 7. The bipartite system viewed from mechanical port of SG1.

be naturally generalized in the port-based approach which turns out to provide additional flexibility in analyzing dynamic interaction from different views.

For instance, we can split the system in Fig. 7 at the T_m-ω (mechanical) port of SG1. The transfer function seen at this port is $G''_{T_{m1}\omega_1}$. We take out the rotor inertia from this port and model the dynamics of the rest parts of the grid as a dynamic torque coefficient $K_{T_{m1}}$

$$K_{T_{m1}} = G''^{-1}_{T_{m1}\omega_1} - sJ_1. \tag{3}$$

The stability of the system is reduced, without loss of detail, to the closed-loop interaction between the rotor inertia $\frac{1}{sJ_1}$ and the *dynamic torque coefficient* $K_{T_{m1}}$, as shown in Fig. 7. $K_{T_{m1}}$ is an extension to the conventional torque coefficient and it encapsulates the dynamics of the entire grid (including EMT of lines and other apparatuses) except the rotor of SG1. If $K_{T_{m1}}$ itself is stable, the whole-system stability can be evaluated by the loop gain of Fig. 7 via Nyquist criterion. Since $\frac{1}{sJ_1}$ has a constant phase shift of -90° along the Nyquist contour, the phase of $K_{T_{m1}}$ should be kept above -90° to ensure positive phase margin, or equivalently, the real part of $K_{T_{m1}}$ should be positive. This leads to a very simple stability index which is very useful in stability analysis and tuning, as will be demonstrated in the case studies later. It is worth mentioning that obtaining the dynamic torque coefficient only needs the prior knowledge of the inertia and the mechanical-port transfer function (mechanical impedance) of the apparatus. The detailed state equations are not required. This features the black-box analysis. As will be shown in Section IV-C later, the dynamic torque coefficient can also be used to identify the participation of apparatus, guide the parameter tuning, and predict the system stability more accurately than conventional algebraic (state-less) torque coefficient in literature.

Similarly, we can also split the system in Fig. 7 at the i_{dc}-v_{dc} (dc-link) port of IBR3. We define the dc-link capacitance as the *electrical inertia* and takes it out from the port transfer function $G''_{i_{dc3}v_{dc3}}$ to yield the closed-loop diagram in Fig. 8, where

$$K_{i_{dc3}} = G''^{-1}_{i_{dc3}v_{dc3}} - sC_3 \tag{4}$$

is called the *dc-current coefficient*. $K_{i_{dc3}}$ plays a similar role to $K_{T_{m1}}$ which is named *generalised torque coefficient* together with $K_{T_{m1}}$.

It is possible to explore other ways of bipartition at different ports, e.g. an exciter port of a SG, or a V-Q control port of an IBR. Additionally, We can also split at multiple ports to investigate oscillations in which multiple apparatuses are participating and identify which apparatus is the dominant one.

C. Practical Implementation

The implementation of the port-based approach relies on numerical calculation of frequency spectra or transfer func-

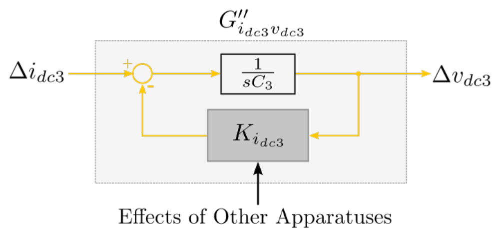

Fig. 8. The bipartite system viewed from dc-link port of IBR3.

tions on the whole-system scale. We developed an open-source toolbox to automate the numerical calculation and visualise the resulted interpretation in a human-understandable pattern [21]. The toolbox also offers cross-validation between port-based analysis, state-space analysis, and time-domain simulation.

The port-based analysis is case-dependant and may generate different results for different grid conditions and scenarios [22]. The toolbox can help scan through a range cases to identify the common features and exceptions via data-driven methods [23], [24]. On the other hand, it is also possible to establish modular criterion on each port to achieve case-independent stability. Several valuable attempts have been made towards this direction, although they are based on some idealised assumptions [9].

IV. Case Studies

In this section, the effectiveness of the port-mapping method is illustrated through stability analysis for three cases. The first two cases, (a) single-SG-infinite-bus system, and (b) single-IBR-weak-grid system, revisit well-known stability concerns in very simple set-ups but with new insights. The third case, (c) modified IEEE 14-bus SG-IBR composite system, illustrates the benefit of the port-mapping method in studying SG-IBR composite systems. The parameters and models of all three cases, generated from the procedures in Section II and Section III, are available at [21].

A. Case 1: Single-SG-Infinite-Bus System

A single-SG-infinite-bus system and the familiar swing-dynamics are used to illustrate the mapping between damping on the mechanical and electrical ports. The line resistance R_b (electrical damping) is increased from 0 pu to 0.3 pu and the corresponding dynamic torque coefficient K_{T_m} is plotted in Fig. 9(a). It is clear that the real part of K_{T_m} becomes negative as R_b increases, implying negative phase margin and negative damping. In other words, the positive damping on the electrical port maps to negative damping on the mechanical port, and the system tends to be unstable, as is confirmed by the pole loci in Fig. 10. By contrast, the conventional torque coefficient in Fig. 9(b) ignores the electrical dynamics, and fails to predict this resistance-induced instability here. This resistance-induced instability itself is also a surprising result and may inspire rethinking on the nature of damping in power systems. That is, the damping on a specific port may not always be helpful for whole-system damping. This phenomenon is named as *double-edged damping* in this article.

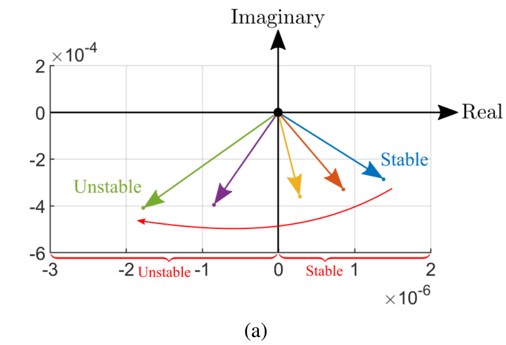

Fig. 9. Case 1: vector diagram of torque coefficient K_{T_m} when increasing the line resistance R_b from 0 pu to 0.3 pu. (a) Dynamic torque coefficient. (b) Conventional state-less torque coefficient when ignoring electrical dynamics of lines.

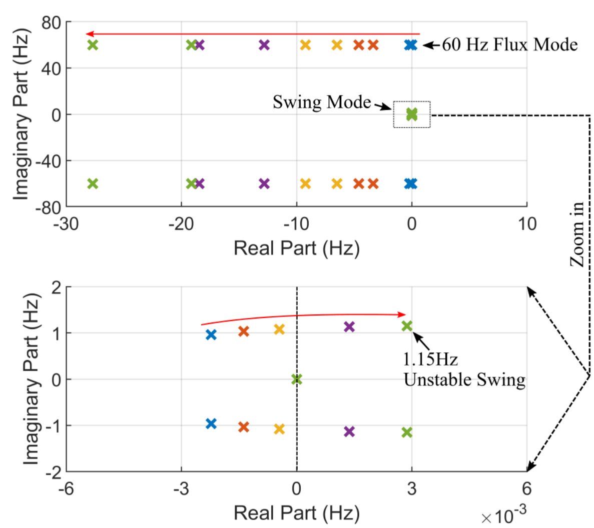

Fig. 10. Case 1: whole-system pole loci with increasing the line resistance R_b from 0 pu to 0.3 pu.

This also explains why a power system stabiliser (PSS) is frequently needed to provide extra damping to the mechanical port [1].

B. Case 2: Single-IBR-Weak-Grid System

It is known that the stability of a grid-following IBR is degraded when connected to a weak grid, i.e., a grid with large impedance and low short-circuit ratio (SCR) [25]. The port-mapping method will again be used to identify how changes at the ac electrical port is mapped to the dc-link port. We select

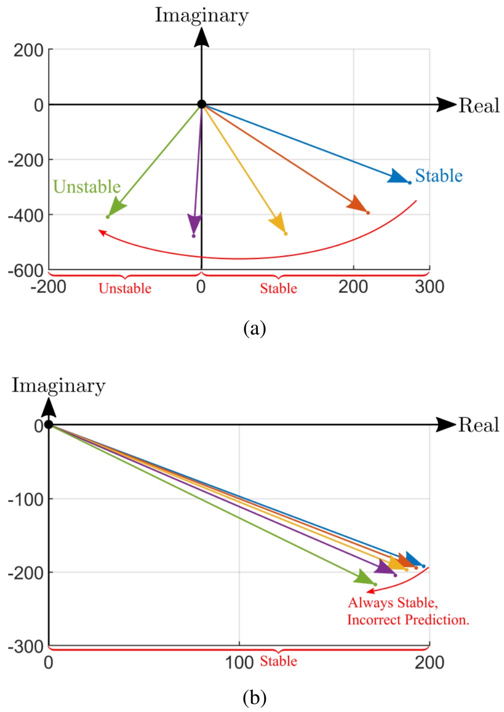

Fig. 11. Case 2: vector diagram of dc-current coefficient $K_{i_{dc}}$ when reducing the SCR from 2.71 to 1.35. (a) Dynamic dc-current coefficient. (b) Steady dc-current coefficient when ignoring electrical dynamics of lines.

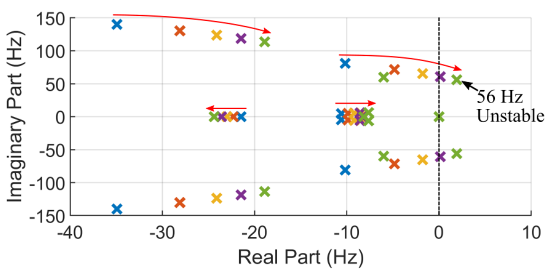

Fig. 12. Case 2: whole-system pole loci when reducing the SCR from 2.71 to 1.35.

the dc-link port for system bipartition and plot the dc-current coefficient $K_{i_{dc}}$ for SCR reducing from 2.71 to 1.35. It is clear from Fig. 11 that the real part of $K_{i_{dc}}$ becomes negative as SCR reduces, indicating the SCR of the ac electrical port maps to positive damping in the dc-link port. Again, this prediction is confirmed by the pole loci in Fig. 12. Again, the steady dc-current coefficient ignores the fast EMT dynamics of grid lines, which leads to large prediction errors because the oscillation frequency here is relatively high (around 56 Hz in Fig. 12). This provides a new interpretation to the stability problem of IBRs connecting to weak grids, and points to the potential solution of inserting extra damping that is similar to a PSS on dc-link control in order to counteract the negative damping, as is explored in [25], [26].

C. Case 3: Modified IEEE 14-Bus SG-IBR Composite System

We now move on to a larger-scale case of a modified IEEE 14-bus power system to investigate the interaction between SGs and IBRs. The same layout of the IEEE standard 14-bus

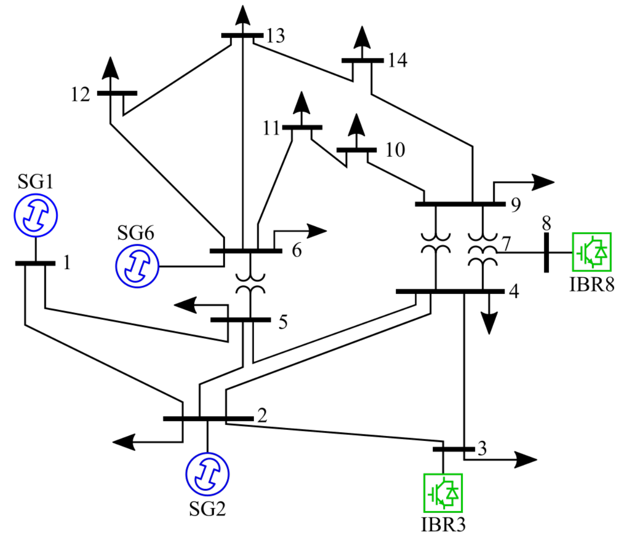

Fig. 13. Case 3: IEEE 14-bus SG-IBR composite power system.

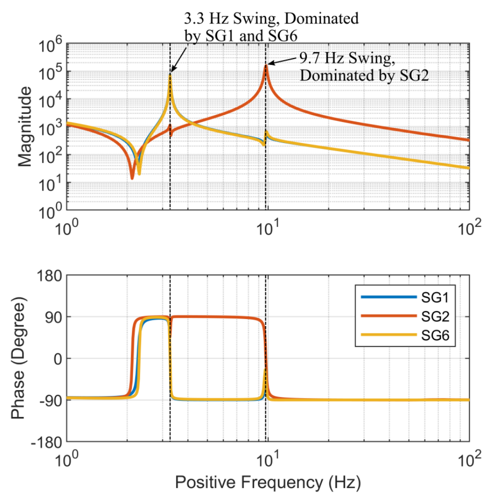

Fig. 14. Case 3: Bode diagram of mechanical port closed-loop transfer function (i.e., the mechanical gain $G''_{T_m\omega}$ in G''_N) for each SG.

system is used but two SGs are replaced by IBRs, as shown in Fig. 13. Through analogy with the electrical impedance analysis in [27], the resonant peaks in frequency spectra of mechanical impedance $G''_{T_m\omega}$ (see Fig. 14) can help to identify the oscillation modes from the mechanical-centric view. More importantly, by comparing the kurtosis of different apparatuses, we can also identify their participation in each mode. It indicates that the 9.7 Hz swing mode is dominated by SG2 (red line), and the 3.3 Hz swing mode is jointly dominated by SG1 (blue line) and SG6 (yellow line). The port-mapping method can be used here again to investigate the interaction between SGs and IBRs. The dynamic torque coefficient K_{T_m} of each machine is shown in Fig. 15, where the bode plot is used so that we can investigate the magnitude and phase of K_{T_m} at both of the swing frequencies in the same figure. It is clear that in each of the K_{T_m} we can only see one of the two swing modes. For instance, in $K_{T_{m6}}$ (yellow line) of SG6, we only see the 9.7 Hz mode, because the 3.3 Hz

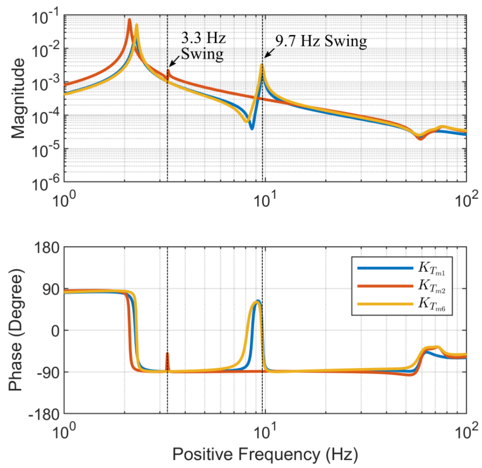

(a)

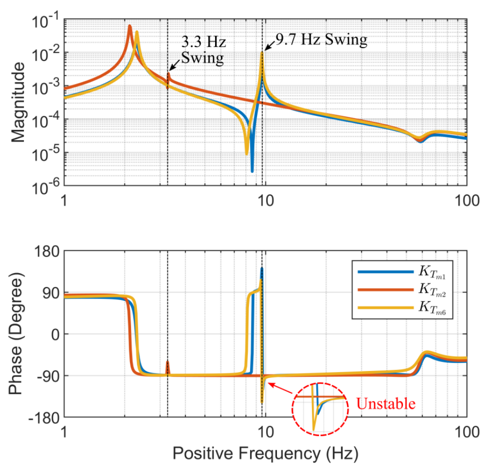

(b)

Fig. 15. Case 3: Bode diagram of torque coefficient K_{T_m} for each SG with changing the power-frequency control bandwidth (dc-link and PLL) of IBRs. (a) Bandwidth of 25 Hz. (b) Bandwidth of 5 Hz.

mode arises from SG6 itself (i.e., interaction between $K_{T_{m6}}$ and J_6) and is therefore hidden if we examine $K_{T_{m6}}$ only by splitting J_6 out of the whole system. This agrees with the participation analysis obtained from mechanical impedance in Fig. 14. It is worth emphasising that, in contrast to the conventional participation factor analysis of a white-box state space model [7], [28], the participation analysis here is based on a black-box transfer function model. In other words, it only needs the prior knowledge of the output characteristics (i.e., transfer functions at output ports) of apparatuses rather than the detailed state equations or state space models. It is worth mentioning that, even though a black-box state-space model can also be derived from the black-box transfer function, this derivation is not a one-to-one mapping. That is to say, the state matrix (A matrix) derived from the black-box transfer function would be different from the state matrix derived from the state equations based on the physics of the system, even though they correspond to a same transfer function. This means the mapping between states and the physical variables would not be present in the derived black-box state space model. In this

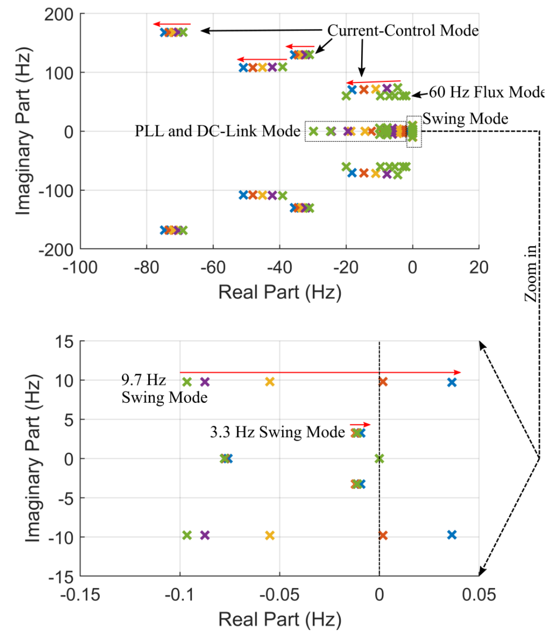

Fig. 16. Case 3: whole-system pole loci with reducing the IBR dc-link and PLL bandwidths from 25 Hz to 5 Hz.

case, the participation factors can still be calculated, but can not be linked to physical variables and can not be used for root-cause analysis.

The damping of $K_{T_{m1}}$ and $K_{T_{m6}}$ is sensitive to the dc-link and PLL control gain of IBRs, which is clear to see by comparing Fig. 15 (a) and (b). For lower dc-link and PLL control bandwidth, the phases of K_{T_m1} and K_{T_m6} both drop below -90° at the 9.7 Hz mode, indicating negative damping for this mode. This means that lower bandwidth of dc-link and PLL control of IBRs may map to negative damping at the mechanical ports of SGs. It has also been proved that slower dc-link and PLL control may induce positive damping of electrical ports [25], [26], [29]. Therefore, this is another example of how damping at different ports contradicts each other, i.e., the double-edged damping. The pole loci in Fig. 16, once more, confirm this prediction.

The corresponding time-domain simulation results are shown in Fig. 17. At 0 s, the IBR power-frequency bandwidth is reduced from 25 Hz to 5 Hz and the unstable 9.7 Hz swing oscillation begins. At 5 s, the mechanical damping torque coefficient K_{D2} of the critical SG2 is increased from 1 pu to 2 pu, which re-stabilizes the system. The simulation results agree with the theoretical prediction.

It is worth emphasising that the focus in this case is not the interaction between PLL and dc-link control of an IBR but instead the focus is the interaction (the power-angle interaction specifically) between IBRs and SGs. Further, unlike a SG whose power angle dynamics are govern by only one port (T-ω port [1]), an IBR's power-angle dynamics are governed by two ports (PLL port for angle/frequency control and dc-link port for power control [26]). This is why bandwidths of both the PLL and the dc-link control of IBRs were changed together in the case studies here.

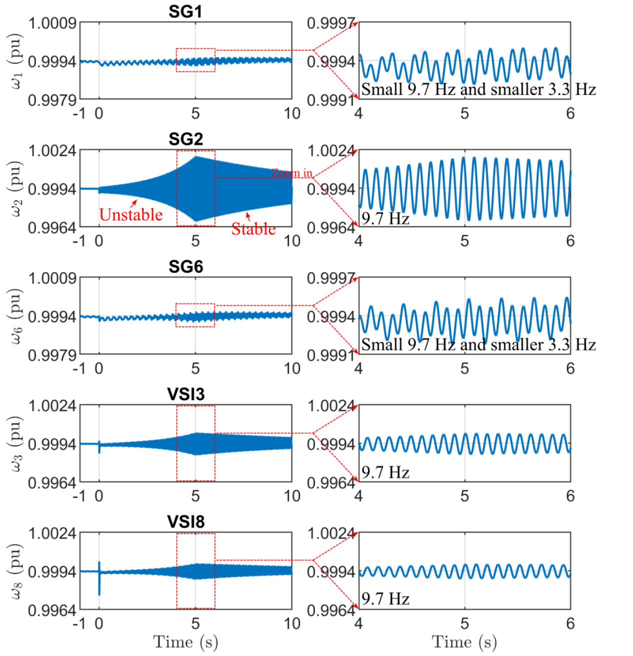

Fig. 17. Case 3: simulation results. At 0 s, the dc-link and PLL bandwidths of IBR are reduced from 25 Hz to 5 Hz, which destabilizes the 9.7 Hz swing mode. At 5 s, the mechanical damping of SG2 is increased from 1 pu to 2 pu, which re-stabilizes the system.

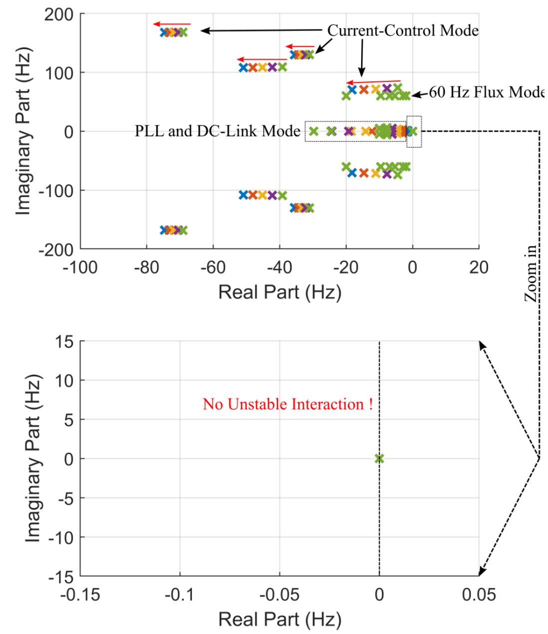

Fig. 18. Case 3 with replacing all SGs by infinite buses: whole-system pole loci with reducing the IBR dc-link and PLL bandwidths from 25 Hz to 5 Hz.

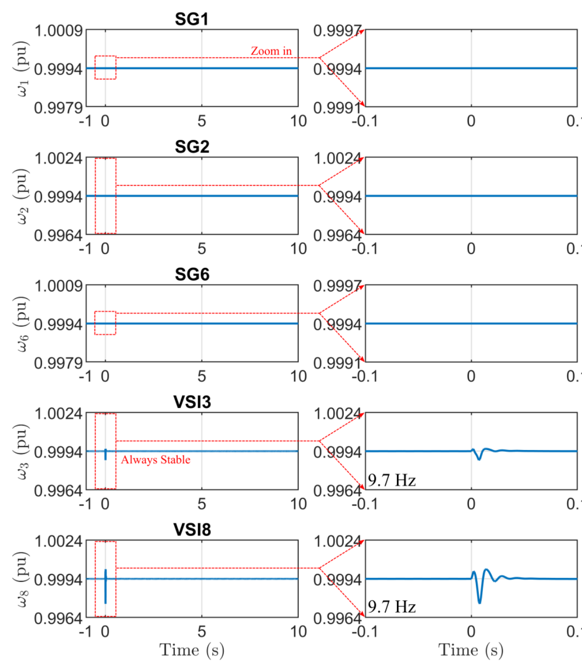

Fig. 19. Case 3 with replacing all SGs by infinite buses: simulation results. At 0 s, the dc-link and PLL bandwidths of IBR are reduced from 25 Hz to 5 Hz.

In order to further validate that the instability is caused by the interaction between IBRs and SGs, we remove the mechanical dynamics of SGs (replacing SG1, SG2, and SG6 by infinite buses) and change IBR bandwidths again. Fig. 18 shows the whole-system pole loci with reducing the IBR bandwidth from 25 Hz to 5 Hz. It can be seen that the current-control mode, the 60 Hz flux mode, the PLL mode, and the dc-link mode all change in a similar manner to Fig. 16 but the unstable swing mode in Fig. 16 is not present in Fig. 18, which means the system is stable. In other words, the IBRs does not interact with infinite buses (which have no mechanical dynamics) but do interact with SGs (which have mechanical dynamics). Fig. 19 shows the time-domain simulation and validates the system is stable under changing IBR bandwidths.

V. Conclusions

A port-mapping method has been put forward for stability analysis of composite power systems with mixtures of SGs and IBRs. It combines the mechanical- and electrical-centric analysis of power systems in a black-box format, i.e., using transfer functions at ports of interest only without the requirement of detailed state equations of each apparatus. The mechanical rotational dynamics are mapped to the electrical impedance or admittance, and meanwhile the electrical dynamics are also mapped to the mechanical impedance and dynamic torque coefficient. This united cross-domain methodology enables more flexible bipartition of power systems to allow for more interpretative investigation into the interaction amongst subsystems, which yields new stability indices such as generalised torque coefficients. Additionally, this article warns that the conventional torque coefficient which ignores fast electrical dynamics of lines or is based on steady electrical phasors might fail to predict the system instability when the line resistance is large or when the oscillation frequency is high. This article also warns that positive damping at certain port might map to a negative damping at another port and worsen the whole-system stability. In other words, the positive damping is not always globally good for the whole-system, i.e., the phenomenon of double-edged damping.

APPENDIX A
STATE EQUATIONS OF SYNCHRONOUS GENERATOR

We use the fourth-order model for a SG which is a minimum model containing both electrical and mechanical dynamics. The corresponding state equations are [17]

$$\begin{aligned} v_d &= \dot{\psi}_d - Ri_d - \omega\psi_q \\ v_q &= \dot{\psi}_q - Ri_q + \omega\psi_d \\ J\dot{\omega} &= T_m - T_e - K_D\omega \\ \dot{\theta} &= \omega \end{aligned} \tag{5}$$

with

$$\psi_d = -Li_d,\ \psi_q = -Li_q - \psi_f,\ T_e = \psi_f i_d \tag{6}$$

where ψ_d and ψ_q are dq-axis flux linkages respectively; ψ_f is the field flux linkage; v_d and v_q are dq-axis stator voltages; i_d and i_q are dq-axis stator currents; θ and ω are the rotor speed and angle; J is the rotor inertia; T_m and T_e are the mechanical and electromagnetic torque respectively; K_D is the damping torque coefficient; R and L are stator resistance and inductance respectively.

APPENDIX B
MODEL DERIVATION OF PORT-MAPPING METHOD

A. $G \to G'$ (Mechanical Dynamics $\to$ Electrical Ports)

According to Fig. 3 (e), the element relationship between G in mechanical frame and G' in electrical frame can be obtained as

$$\begin{aligned} G'_{vi} &= T_{\epsilon_0}\left(G_{vi} + (I_0 - G_{vi}V_0)\underbrace{(s + G_{v\omega}V_0)^{-1}G_{v\omega}}_{G'_{v\omega}T_{\epsilon_0}/s}\right)T_{\epsilon_0}^{-1} \\ G'_{Ti} &= T_{\epsilon_0}\left(G_{Ti} + (I_0 - G_{vi}V_0)\underbrace{(s + G_{v\omega}V_0)^{-1}G_{T\omega}}_{G'_{T\omega}/s}\right) \\ G'_{v\omega} &= \left(s(s + G_{v\omega}V_0)^{-1}G_{v\omega}\right)T_{\epsilon_0}^{-1} \\ G'_{T\omega} &= s(s + G_{v\omega}V_0)^{-1}G_{T\omega} \end{aligned} \tag{7}$$

where $I_0 = [-i_{q0}; i_{d0}]$ and $V_0 = [-v_{q0}; v_{d0}]$ are the steady-state operating points at the electrical port; T_{ϵ_0} is the frame transformation matrix with the steady-state angle ϵ_0. The first equation in (7) builds the relationship between G_{vi} (admittance in mechanical frame) and G'_{vi} (admittance in electrical frame) by embedding the mechanical dynamics into electrical ports, which corresponds to the impedance-based analysis in [17], [19] albeit that they focus on the electrical domain only.

B. $G' \to G''$ (Electrical Dynamics $\to$ Mechanical Ports)

According to Fig. 3 (e), the element relationship between G' (apparatus model with embedding mechanical dynamics into electrical ports) and G'' (model with mapping electrical dynamics back to mechanical ports) can be obtained as

$$\begin{aligned} G''_{vi} &= (I - G'_{vi}Z_b)^{-1}G'_{vi} \\ G''_{Ti} &= (I - G'_{vi}Z_b)^{-1}G'_{Ti} \\ G''_{v\omega} &= G'_{v\omega} + G'_{v\omega}Z_b\underbrace{(I - G'_{vi}Z_b)^{-1}G'_{vi}}_{G''_{vi}} \\ G''_{T\omega} &= G'_{T\omega} + G'_{v\omega}Z_b\underbrace{(I - G'_{vi}Z_b)^{-1}G'_{Ti}}_{G''_{Ti}} \end{aligned} \tag{8}$$

REFERENCES

[1] P. Kundur, *Power system stability and control*. McGraw-hill New York, 1994, vol. 7.

[2] C. L. DeMarco, "Design of predatory generation control in electric power systems," in *Proceedings of the Thirty-First Hawaii International Conference on System Sciences*, vol. 3. IEEE, 1998, pp. 32–38.

[3] F. Blaabjerg, R. Teodorescu, M. Liserre, and A. V. Timbus, "Overview of control and grid synchronization for distributed power generation systems," *IEEE Trans. Ind. Electron.*, vol. 53, no. 5, pp. 1398–1409, Oct. 2006.

[4] Y. Gu, Y. Li, H.-J. Yoo, T.-T. Nguyen, X. Xiang, H.-M. Kim, A. Junyent-Ferre, and T. C. Green, "Transfverter: Imbuing transformer-like properties in an interlink converter for robust control of a hybrid ac–dc microgrid," *IEEE Trans. Power Electron.*, vol. 34, no. 11, pp. 11 332–11 341, 2019.

[5] J. Shair, X. Xie, L. Wang, W. Liu, J. He, and H. Liu, "Overview of emerging subsynchronous oscillations in practical wind power systems," *Renewable and Sustainable Energy Reviews*, vol. 99, pp. 159–168, 2019.

[6] J. Bialek, "What does the GB power outage on 9 august 2019 tell us about the current state of decarbonised power systems?" *Energy Policy*, vol. 146, p. 111821, 2020.

[7] U. Markovic, O. Stanojev, P. Aristidou, E. Vrettos, D. S. Callaway, and G. Hug, "Understanding small-signal stability of low-inertia systems," *IEEE Trans. Power Syst.*, Early Access.

[8] S. Curi, D. Groß, and F. Dörfler, "Control of low-inertia power grids: A model reduction approach," in *2017 IEEE 56th Annual Conference on Decision and Control (CDC)*. IEEE, 2017, pp. 5708–5713.

[9] R. Pates and E. Mallada, "Robust scale-free synthesis for frequency control in power systems," *IEEE Transactions on Control of Network Systems*, vol. 6, no. 3, pp. 1174–1184, 2019.

[10] D. Zonetti, "Energy-based modelling and control of electric power systems with guaranteed stability properties," Ph.D. dissertation, Université Paris-Saclay, 2016.

[11] Y. Wang, X. Wang, Z. Chen, and F. Blaabjerg, "Small-signal stability analysis of inverter-fed power systems using component connection method," *IEEE Trans. Smart Grid*, vol. 9, no. 5, pp. 5301–5310, Sep. 2018.

[12] R. Middlebrook, "Null double injection and the extra element theorem," *IEEE Transactions on Education*, vol. 32, no. 3, pp. 167–180, 1989.

[13] J. Liu, X. Feng, F. C. Lee, and D. Borojevich, "Stability margin monitoring for DC distributed power systems via perturbation approaches," *IEEE transactions on power electronics*, vol. 18, no. 6, pp. 1254–1261, 2003.

[14] Y. Gu, W. Li, and X. He, "Passivity-based control of DC microgrid for self-disciplined stabilization," *IEEE Transactions on Power Systems*, vol. 30, no. 5, pp. 2623–2632, 2015.

[15] L. Harnefors, "Modeling of three-phase dynamic systems using complex transfer functions and transfer matrices," *IEEE Trans. Ind. Electron.*, vol. 54, no. 4, pp. 2239–2248, Aug. 2007.

[16] Y. Li, Y. Gu, Y. Zhu, A. Junyent-Ferré, X. Xiang, and T. C. Green, "Impedance circuit model of grid-forming inverter: Visualizing control algorithms as circuit elements," *IEEE Transactions on Power Electronics*, vol. 36, no. 3, pp. 3377–3395, 2021.

[17] Y. Gu, Y. Li, and T. C. Green, "Impedance-based whole-system modeling for a composite grid via embedding of frame-dynamics," *IEEE Trans. Power Syst.*, vol. 36, no. 1, pp. 336–345, Jan. 2021.

[18] Y. Liao and X. Wang, "Mathematical relationships of linearized modeling methods of ac power electronic systems," 2021.

[19] Y. Li, Y. Gu, and T. C. Green, "Interpreting frame transformations in ac systems as diagonalization of harmonic transfer functions," *IEEE Trans. Circuits Syst. I, Reg. Papers,*, vol. 67, no. 7, pp. 2481–2491, Jul. 2020.

[20] R. L. Boylestad, *Introductory circuit analysis*. Prentice Hall Press, 2010.

[21] "Future Power Networks." [Online]. Available: https://github.com/Future-Power-Networks/Publications

[22] R. Henriquez-Auba, J. D. Lara, C. Roberts, N. Pallo, and D. S. Callaway, "Lits. jl–an open-source julia based simulation toolbox for low-inertia power systems," *arXiv preprint arXiv:2003.02957*, 2020.

[23] J. Yi, W. Lin, J. Hu, J. Dai, X. Zhou, and Y. Tang, "An integrated model-driven and data-driven method for on-line prediction of transient stability of power system with wind power generation," *IEEE Access*, vol. 8, pp. 83 472–83 482, 2020.

[24] T. Thobias, A. Rathinam, B. Saravanan, and S. Senthilmurugan, "Data-driven power system stability analysis for enhanced situational awareness," in *Cognitive Informatics and Soft Computing*. Springer, 2021, pp. 799–816.

[25] Y. Huang, X. Yuan, J. Hu, and P. Zhou, "Modeling of vsc connected to weak grid for stability analysis of dc-link voltage control," *IEEE Journal of Emerging and Selected Topics in Power Electronics*, vol. 3, pp. 1193–1204, 2015.

[26] H. Yuan, X. Yuan, and J. Hu, "Modeling of grid-connected vscs for power system small-signal stability analysis in dc-link voltage control timescale," *IEEE Trans. Power Syst.*, vol. 32, no. 5, pp. 3981–3991, 2017.

[27] Y. Zhu, Y. Gu, Y. Li, and T. C. Green, "Participation analysis in impedance models: The grey-box approach for power system stability," *IEEE Trans. Power Syst.*, Early Access.

[28] N. Pogaku, M. Prodanovic, and T. C. Green, "Modeling, analysis and testing of an inverter-based microgrid," *IEEE Trans. Power Electron.*, vol. 22, no. 2, pp. 613–625, Mar. 2007.

[29] B. Wen, D. Boroyevich, R. Burgos, P. Mattavelli, and Z. Shen, "Analysis of dq small-signal impedance of grid-tied inverters," *IEEE Transactions on Power Electronics*, vol. 31, no. 1, pp. 675–687, 2016.